Journal of Materials Chemistry A

Accepted Manuscript

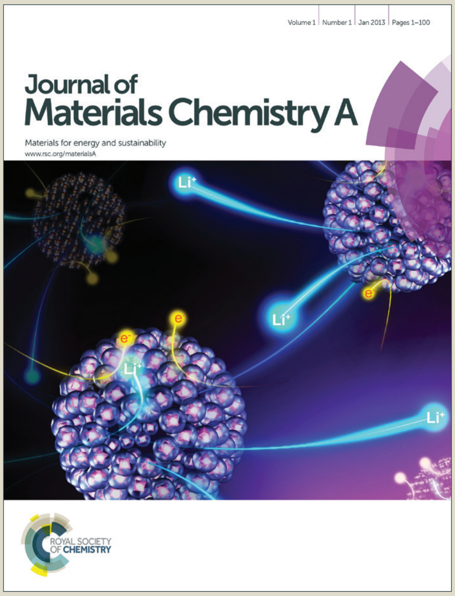

ROYAL SOCIETY OF CHEMISTRY

www.rsc.org/materialsA

Journal Name RSCPublishing

COMMUNICATION

Cite this: DOI: 10.1039/x0xx00000x

An In-Situ and General Preparation Strategy for Hybrid Metal/Semiconductor Nanostructures with Enhanced Solar Energy Utilization Efficiency

Received 00th January 2012,
Accepted 00th January 2012

DOI: 10.1039/x0xx00000x

www.rsc.org/

Hua Bai,[a] Fang Ye,[a] Qing Lv,[a] Guangcheng Xi,*[a] Junfang Li,[a] Haifeng Yang,[a] and Chongqing Wan*[b]

Hybrid metal/semiconductor nanostructures have been synthesized by an general in-situ reaction between weakly reductive metal oxides and oxidative metal precursors without foreign reducing agents and stabilizing agents. The hybrid materials exhibit excellent activity for photocatalytic generation of benzyl compounds.

Metal nanoparticles of various sizes and morphologies have many areas of application, including catalysis[1,2], chemical sensing[3], biolabelling[4,5], electronics[6], and surface enhanced Raman spectrum[7]. For example, Metal catalysts with finite nanoparticle size have been found to be very active for specific reactions in dark conditions such as CO oxidation.[8,9] Their preparation often involves colloidal sols with a well-defined particle size distribution, in which the nanoparticles are stabilized in solution by the adhesion of specific surfactant or ligand molecules, which ensure that the nanoparticles cannot coalesce.[10] The stabilized nanoparticles are then typically deposited onto a solid surface to enable them to have utility in a chosen application.[11]

Recently, metal nanoparticles as important co-catalysts, have been intensively investigated in semiconductor photocatalysis, such as hydrogen generation, reduction of carbon dioxide, dye degradation, and organic synthesis.[12-17] The photocatalytic process involves excitation of a semiconductor with photons of equal or higher energy than the band gap energy producing electron–hole pairs. These pairs either recombine or react with adsorbed species. An effective photocatalyst is one that can use these electrons and holes efficiently.[18] The presence of metal nanoparticles not only can trap the photo-excited electrons from the conduction band and transfer them to the adsorbed species,[19,20] but also can dramatically improve light harvest attributed to the well-known localized surface plasmon resonance (LSPR) effect.[21] The presence of an obstacle on the interface, such as surfactants and polymers, will seriously hinder the direct charge transfer or dramatically decrease the intensity of LSPR-induced electromagnetic field close to semiconductor, as this field decays exponentially with distance.[22]To date, thoroughly removal of these stabilizing molecules has been achieved only by using thermal and oxidative methods.[23] Such methods inevitably lead to significant morphology changes and size increasing of the hybrid materials, in turn altering their catalytic activity.[24]

Alternatively, if metal nanoparticles could be directly grown over a semiconductor substrate through an in-situ growth procedure without any foreign reducing agents and stabilizing molecules, the catalytic activity of the resulting hybrid nanostructures would be significantly enhanced. Herein, we report a novel, simple, and clean method for the direct growth of noble metal (Ag, Au, Pt, Pd) nanoparticles on metal oxide (MoO_3, V_2O_5, TiO_2) nanostructures through an in-situ oxidation-reduction reaction between weakly reductive non-stoichiometric metal oxides (MoO_{3-x}, V_2O_{5-x}, TiO_{2-x}) and oxidative noble-metal precursors ($AgNO_3$, $HAuCl_4$, H_2PtCl_6, $PdCl_2$) in aqueous solution at room temperature. No foreign reducing agents or stabilizing agents are required, avoiding the introduction of impurities and ensuring that the metal/semiconductor interfaces are clean. Furthermore, compared with only UV-active pure MoO_3, these hybrid metal/MoO_3 nanobelts exhibit excellent visible-light photocatalytic activity and very high stability for degradation of a three kinds of azo dyes and photocatalytic synthesis of five kinds of benzyl compounds. We believe that this approach can be extended to the synthesis of other metal/semiconductor hybrid materials.

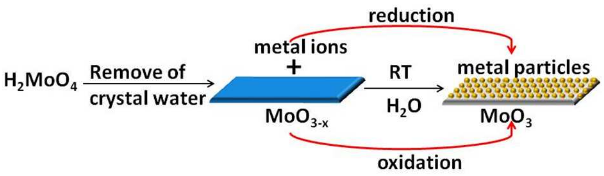

Fig. 1 Schematic Procedure for in-Situ Loading of Metal nanoparticles on MoO$_3$ nanobelts.

We use synthesis of metal/MoO$_3$ nanostructures as an example to illustrate this novel method. The general pathway used to in-situ fabricate metal/MoO$_3$ hybrid nanobelts is shown in Fig. 1. Our inspiration raise from the following idea: for most types of transition metal oxides, their low valence state or nonstoichiometric species often have strong or weak reducing power due to the presence of oxygen vacancies. Therefore, we could first synthesize a low-valence-state or nonstoichiometric species of a metal oxide with a desirable morphology. The reductive metal oxide nanostructures with large quantity of oxygen vacancies could then react with the oxidative noble-metal precursors in aqueous solution. In the present case, metal/MoO$_3$ hybrid nanostructures were prepared in two steps: (1) H$_2$MoO$_4$ was first used to synthesize the MoO$_{3-x}$ nanobelts by a surfactant-free hydrothermal method, which has a reducing ability attributed to the large quantity of oxygen vacancies; (2) the as-synthesized MoO$_{3-x}$ nanobelts and noble metal precursors (AgNO$_3$, HAuCl$_4$, H$_2$PtCl$_6$, PdCl$_2$) were then mixed in aqueous solution at room temperature. Once the metal ions come into contact with the reductive MoO$_{3-x}$ nanobelts, they are immediately reduced and nucleated rapidly on substrate, growing into clusters and further into nanoparticles. Meanwhile, the MoO$_{3-x}$ support was oxidized by the metal ions and converted into MoO$_3$, resulting metal/MoO$_3$ nanocomposites. Compared with previously reported in-situ thermal decomposition method (330 °C) for the synthesis of Ag/MoO$_3$ nanorods,[25] the present room-temperature solution method obviously having more maneuverability and controllability.

Early, Lou et al. created a serious of solution-phase method for the synthesis of orthorhombic MoO$_3$ nanorods and nanobelts.[26-28] Here, the reductive MoO$_{3-x}$ nanobelts were prepared by hydrolyzing molybdic acid (H$_2$MoO$_4$) in acidic aqueous solution followed by hydrothermal treatment (see experimental section, ESI†). Unlike white MoO$_3$, the obtained MoO$_{3-x}$ products display vivid blue color (Fig. S1a, ESI†), which were quite stable in air and could maintain the blue color for several months. It has been well explained that many blue color of transition metal oxides results from the characteristic outer d-orbit electrons, including oxygen vacancy-rich WO$_{3-x}$ nanowires[29] and TiO$_{2-x}$ nanocrystals.[30]

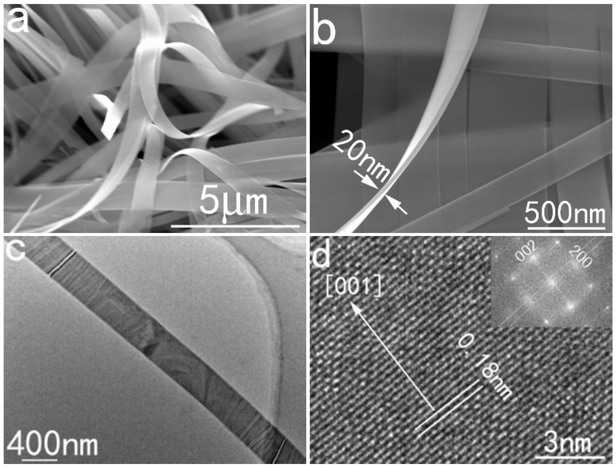

Fig. 2 (a,b) SEM images of the MoO$_{3-x}$ products. (c) TEM image of the MoO$_{3-x}$ nanobelts. (d) HRTEM image and corresponding FFT pattern (inset) of the MoO$_{3-x}$ nanobelts.

A typical X-ray powder diffraction (XRD) pattern recorded from the blue sample is shown in Fig. Fig. S1b, ESI†. All of the diffraction peaks can be indexed to the orthorhombic phase molybdenum oxide (JCPDS No. 5-0508). This compound is crystallized in a layered structure composed of MoO$_6$ octahedra by sharing edges and corners (inset in Fig. 2b). No crystalline impurity peaks can be detected from the XRD pattern. The scanning electron microscopy (SEM) image shows that the as-synthesized MoO$_{3-x}$ presents a well-defined belt-like nanostructure (Fig. 2a). The nanobelts are 400−900 nm in width and tens of micrometers in length. High-magnification SEM image (Fig. 2b) reveals that the thickness of the belts is about 20 nm. Transmission electron microscopy (TEM) image further confirms the products in the shape of nanobelts (Fig. 2c). High resolution Transmission electron microscopy (HRTEM) image (Fig. 2d) and the corresponding FFT pattern (inset in Fig. 2d) confirm the nanobelts grown along the [001] direction. Energy-dispersive X-ray spectroscopy (EDS) confirms that the sample contains only the elements Mo and O (Fig. S2, ESI†). In addition, the Fourier transform IR (FTIR) spectrum exhibits no organics coated on the surface of the MoO$_{3-x}$ nanobelts (Fig. S3, ESI†).

To elucidate the oxidation state of Mo in the blue MoO$_{3-x}$ nanobelts, X-ray photoelectron spectroscopy (XPS) measurements were carried out. Fig. S4 in ESI† displays the Mo 3d XPS core spectra of the as-prepared blue MoO$_{3-x}$ nanobelts and commercial MoO$_3$ powders. As can be seen, only Mo^{6+} exists in the commercial MoO$_3$, whereas both Mo^{6+} and Mo^{5+} are present in the MoO$_{3-x}$ nanobelts. For the commercial MoO$_3$, two peaks (232.9 and 236.1 eV) are attributed to the 3d5/2 and 3d3/2 of Mo^{6+}, respectively.[31] As for the blue MoO$_{3-x}$, the peaks of Mo 3d5/2 and 3d3/2 shift to lower binding energies, and both of them can be divided into two separate peaks. The peaks at 232.9 and 236.1 eV correspond to Mo^{6+}, and those centered at 231.9 and 234.9 eV are assigned to Mo^{5+}. According to the XPS peak area of Mo 3d, the Mo^{6+} and Mo^{5+} cations account for 69.1% and 30.9% of the total Mo states, respectively, in the blue MoO$_{3-x}$ nanobelts. The average oxidation state of Mo is thus determined to be 5.68, which is manifestly the mixed-valence state arising from the oxygen vacancies. The XPS characterization clearly demonstrated that a large quantity of oxygen-vacancy defects contains in the blue MoO$_{3-x}$ nanobelts.

The as-synthesized MoO$_{3-x}$ nanobelts were then reacted with noble metal precursors in aqueous solution at room temperature. As reduction reaction active sites, the contained oxygen vacancies were uniformly distributed in the surface and interior of the MoO$_{3-x}$ nanobelts, and therefore, we can expect that the produced metal nanoparticles are also uniformly distributed on the surface of the whole nanobelts. Fig. 3a-c shows representative SEM and TEM images of the as-synthesized MoO$_3$ nanobelts loaded with 6.3 mol% of Ag nanoparticles. The molar percentage of the loaded metal nanoparticles, which refers to the amount added during preparation, is defined relative to the number of moles of Mo. The SEM and TEM images clearly display that the Ag nanoparticles are homogeneously distributed in the whole MoO$_3$ nanobelt substrate, and their sizes are in the range of 2–5

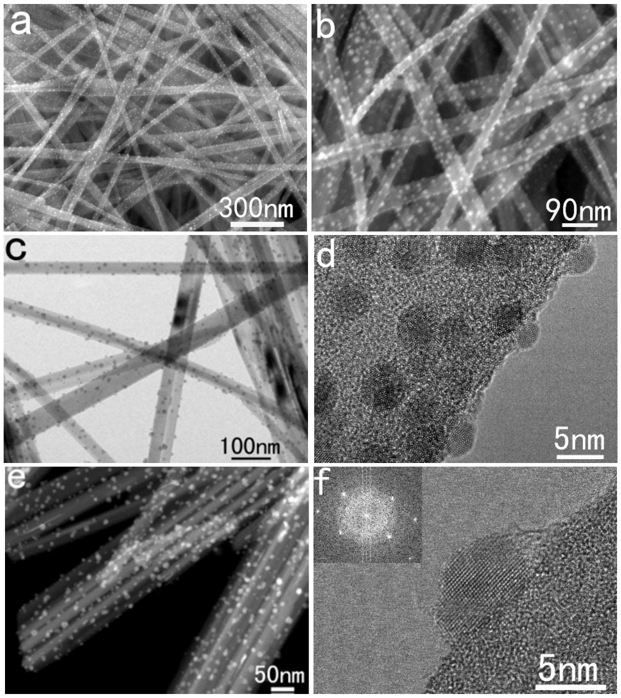

Fig. 3 SEM (a,b), TEM (c,d), and HAADF-STEM (e) images of the obtained Ag/MoO_3 nanobelts. (f) HRTEM images and corresponding FFT pattern of the Ag nanoparticles.

nm according to the high-magnification TEM image (Fig. 3d). The high-angle annular dark-field scanning TEM (HAADF-STEM) image (Fig. 3e) also clearly shows the as-obtained Ag/MoO_3 hybrid nanobelts (the brighter contrast demonstrates Ag). The crystalline nature of the loaded Ag nanoparticles is corroborated by the HRTEM image (Fig. 3f) and corresponding FFT pattern (inset in Fig. 3f). The EDS mapping results (Fig. S5, ESI†) further confirm the composition of an individual Ag/MoO_3 hybrid nanobelt.

We also prepared Au/MoO_3, Pt/MoO_3, and Pd/MoO_3 hybrid nanobelts using the in-situ growth method described above. TEM images of these samples (Fig. 4a-f) show that the surfaces of MoO_3 nanobelts are decorated with numerous nanoparticles having an ultrathin size and a very narrow size distribution. The EDS spectra shown in Fig. S6 confirm that the samples contain only Mo, O, and the corresponding metal elements. The as-synthesized hybrid composites can be easily isolated and re-dispersed in appropriate solvents such as water and ethanol for applications.

Furthermore, we also prepared well-defined Ag/V_2O_5 hybrid nanowires (Fig. 4g) and Ag/TiO_2 nanoplates (Fig. 4h) by using V_2O_{5-x} nanowires and TiO_{2-x} nanoplates as the reductive precursors, respectively. Similar to the hybrid Ag/MoO_3 nanobelts, for the hybrid V_2O_{5-x} nanowires and TiO_{2-x} nanoplates, the metal nanoparticles also very uniformly covered in the nanowires and nanoplates. HRTEM images demonstrated that the Ag nanoparticles are high crystalline. The results showed that noble metal nanoparticles can be generally grown on different semiconductor supports with different morphologies by this oxygen-vacancy-induced in-situ redox route.

Surprisingly, we noted that the widths of the obtained metal/MoO_3 nanobelts range from 30 nm to 80 nm, which are very smaller than those of the original MoO_{3-x} nanobelts (400-900 nm). What happened during the metal nanoparticles loading process? To answer this question, we have systematically surveyed the growth process of the Ag/MoO_3 nanostructures by analyzing samples at different growth stages. Fig. S7 in ESI† shows the SEM images of four samples taken at different stages of the reaction: a) 0, b) 6 h, c) 12, and d) 24 h. These images clearly exhibit the evolution of Ag/MoO_3 hybrid nanobelts from wide to thin over time in aqueous solution. The detailed growth process of the Ag/MoO_3 nanobelts may be described as follows. After 6 h reaction, a large amount of Ag nanoparticles was generated in the nanobelt supports (Fig. S7b); at the same time, many small cracks appeared in the nanobelts (marked with arrows in Fig. S7b). After 12 h reaction, these cracks become more apparent, and some thin Ag/MoO_3 nanobelts have completely split off from the original nanobelts (Fig. S7c). Finally, after 24 h reaction, the original MoO_{3-x} nanobelts completely transformed into thin Ag/MoO_3 nanobelts (Fig. S7d). Interestingly, it is easy to be noted that all of the cracks were formed along the [010] direction. It is well-known that orthorhombic molybdenum oxide has a unique layered structure (Fig. S7e), in which distorted MoO_6 octahedra share four corners to form a plane and two planes join together by sharing octahedral edges to form a single layer. The layers stack up along the [010] direction by van der Waals forces. Due to the weak interaction of van der Waals forces, the layers are easy to be separated along the [010] direction when the chemical environment changes. Therefore, the wide nanobelts

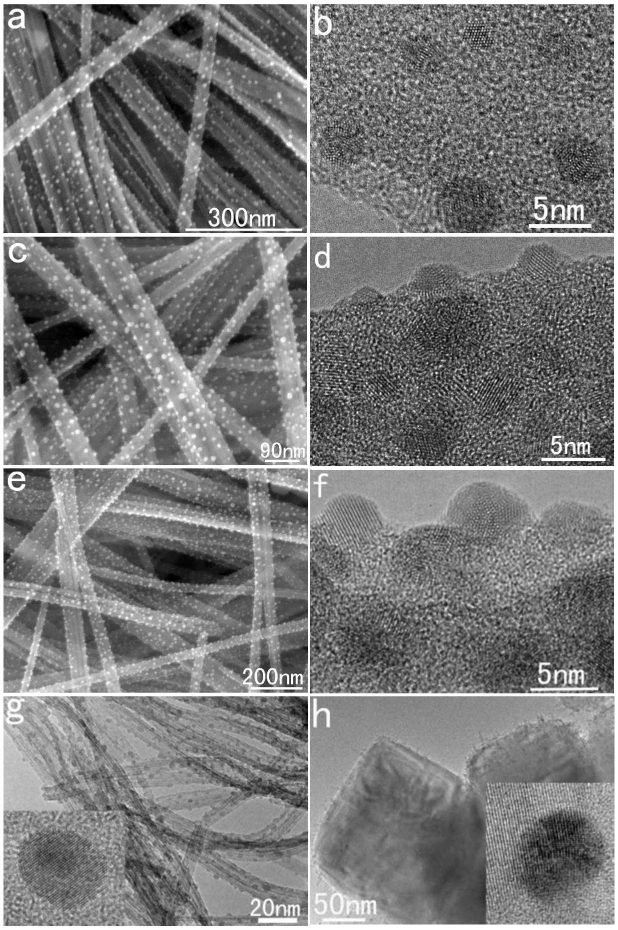

Fig. 4 SEM and HRTEM images of the obtained (a,b) Au/MoO_3, (c,d) Pt/MoO_3, and (e,f) Pd/MoO_3. (g) TEM and HRTEM (inset) images of the obtained Ag/V_2O_5 nanowires. (h) TEM and HRTEM (inset) images of the obtained Ag/TiO_2 nanoplates. The results indicates the generality of the in-situ-growth protocol in generating metal/semiconductor hybrid nanostructures.

separated into thin nanobelts along the direction of weakest intermediate force when they reacted with noble metal precursors. Furthermore, when a larger amount of $AgNO_3$ was added into the reaction system, a lot of Ag/MoO_3 nanowires were obtained, which indicate that the size of the final products can be conveniently controlled by adjusting the precursor concentrations (Figure S8). From the view point of catalysis, the transformation from large size to small size is favorable since their surface areas are greatly increased. This conversion process was illustrated in Fig. S7f.

XPS measurements were then performed to determine thechemical states as-synthesized Ag/MoO_3 hybrids. The survey XPS of the hybrids (Fig. S9a) clearly indicates the presence of Ag and Mo. As can be seen from the Ag XPS spectrum (Fig. S9b), the peaks at 374.6 and 368.5 eV are attributed to the 3d3/2 and 3d5/2 binding energies of zerovalent state of metallic Ag, respectively. We compared the XPS spectra of the Ag/MoO_3 hybrids and the original MoO_{3-x} nanobelts, two peaks can be identified from the O1s core level spectra shown in Fig. S9c: one peak at 530.1 eV is deemed as the oxygen bond of Mo-O-Mo, while the other located at 531.7 ev can be attributed to the O-atoms in the vicinity of an O-vacancy. However, their peak area of 531.7 ev is different, which indicates that the Ag/MoO_3 nanobelts possess much less O-vacancies compared with the original blue MoO_{3-x} nanobelts. Moreover, only Mo^{6+} was observed in the Ag/MoO_3 nanobelt, while a large number Mo^{5+} was observed in the MoO_{3-x} nanobelts (Fig. S9d). The changes in valences of the molybdenum oxide nanobelts before and after the metal loading clearly demonstrated that the Vo-rich MoO_{3-x} nanobelts was oxidized by the oxidative Ag^+ ions and converted into MoO_3 nanobelts, while the Ag^+ ions was reduced into Ag nanoparticels by the reductive Vo-rich MoO_{3-x} nanobelts.

Fig. S10 gives the UV–Vis-NIR absorption spectra of the Au/MoO_3 nanobelts, Ag/MoO_3 nanobelts, and MoO_{3-x} nanobelts. Compared with the MoO_{3-x} nanobelts, the hybrid nanobelts exhibit greatly enhanced absorption from visible to NIR region, which demonstrated that the metal nanoparticles loaded MoO_3 hybrid nanobelts possess strong LSPR effect. Furthermore, the absorption peak of the metal/MoO_3 hybrid nanobelts synthesized by the in-situ growing method is much stronger than that of the metal/semiconductor materials obtained by the traditional synthetic route (Fig. S11a). Fig. S11b shows the TEM image of the Au/MoO_3 obtained the traditional immobilization-high temperature oxidation method. From this image, we can see that the size distribution of the Au nanoparticles is broad, from 2-3 nm to 20 nm. Some groups reported that the narrow particle size distribution is contribute to the formation of narrow and strong absorption peaks.[32,33]

The use of visible light in photochemical synthesis is fundamentally challenging because organic molecules tend not to interact with the wavelengths of visible light that are most strongly emitted in the solar spectrum. Benzyl compounds are important organic intermediates, and widely used in the production of medicines, liquid crystals, and insecticides. Currently, the synthesis of benzyl compounds is often conducted at high temperatures. LSPR effects often give rise to unexpected results in photochemical reactions.[34-39] For example, Wang group reported that metal/semiconductor hybrids display novel photocatalytic properties.[35] We investigated the photocatalytic activity of the Ag/MoO_3 nanobelts in the carbon-nitrogen coupling reaction for the synthesis of benzalaniline compounds, the simplest and most important benzyl aromatic amine, under visible light irradiation. As expected, we were pleasant to find that the Ag/MoO_3 nanobelts achieved highly efficient benzalaniline production according to reaction (shown in Fig. 5) with visible light illumination ($\lambda \geq 420$ nm). The color of the reaction mixture changed into crimson from the original colorless (Fig. S12, ESI†). When 20 mg catalyst was added into the reaction cell, the average formation rate of benzalaniline is about 112 μmol h^{-1} g^{-1} (Fig. 5). Besides benzalaniline, only 4% (molar ratio) of other hydrocarbons (such as aromatic azo and acetone) were produced, which suggests that the selectivity of this coupling reaction is very high. After 40 h reaction, the yield of benzalaniline is up to 95%.

Due to the wide light absorption of the plasmonic Ag/MoO_3 nanobelts, the temperature of the reaction mixtures was found to rise to 50 °C under light irradiation. To distinguish the contribution of this thermal effect, a comparative experiment at 50 °C was carried out with Ag/MoO_3 nanobelts in the dark. The average benzalaniline yield rate in the dark at 50 °C was 22 μmol h^{-1} g^{-1}, which was a little higher than the production at room temperature (25 °C, 8 μmol h^{-1} g^{-1}) and much lower than that under light irradiation (112 μmol h^{-1} g^{-1}). Furthermore, when catalyst was not added, no benzalaniline was obtained from the reaction system under visible light irradiation. So, the benzalaniline generation enhancement upon light irradiation is predominantly due to the plasmonic photocatalysis of the hybrid photocatalysts, and photothermal effect only accounts for a small portion. More important, the new photocatalysts also showed high conversion activities in the highly selective preparation of other more complex benzyl compounds from the corresponding aniline compounds and toluene (see Table 1).

The photocatalytic activities of the as-synthesized metal/MoO_3 samples were also evaluated for degradation of rhodamine B (RhB) under visible-light irradiation ($\lambda \geq 420$ nm), and the results were compared with RhB photolysis (without photocatalyst) and with those obtained over commercial MoO_3 and TiO_2 (P25) (Fig. S13). Within 60 min of visible-light irradiation, the percentages of RhB degraded by commercial MoO_3 and P25 were only 1.5 and 9.1 %, respectively. Significantly larger percentages of RhB were degraded with the Ag/MoO_3, Au/MoO_3, and Pt/MoO_3 samples. More importantly, the metal/MoO_3 nanobelts obtained by the room temperature in-situ method show better photocatalytic efficiency compared with that of Au/MoO_3 obtained by the traditional immobilization-high temperature oxidation method. In addition, for the degradation of methyl orange (MO) and methylene blue (MB), the hybrid materials also showed enhanced visible-light activities. It was observed that the photolysis of RhB under visible-light irradiation was very slow and that RhB cannot be degraded under dark conditions in the presence of the photocatalysts, confirming that the photocatalytic activity indeed originates from the metal/MoO_3 hybrid materials. The enhanced visible-light photocatalytic efficiency may be attributed to the stronger LSPR effect of the metal/MoO_3 hybrid materials (Fig. S10-11).[14] However, the enhanced visible-light photocatalytic properties of Pt/MoO_3 might not result from the SPR effect because no SPR band was found in Pt nanoparticles. From Figure S10 we can see that the MoO_{3-x} nanobelts show a obvious visible absorption due to the oxygen vacancies. Therefore, the enhanced photocatalytic activities of Pt/MoO_3 probably result from the visible absorption of the nanobelt itself. At the same time, the high electron conductivity of the metal nanoparticles also helps to improve the photogenerated electron/hole separation process.[39]

In addition to efficiency, stability and recyclability of photocatalysts are also important for applications. After the RhB molecules are completely decomposed, centrifuging the solution enables the hybrid catalysts to be easily collected to catalyze a new reaction. Fig. S14 plots the kinetic curves for degradation of RhB solution with the use of the same experimental conditions. The Ag/MoO_3 photocatalyst can be effectively recycled at least five times without an apparent decrease in its photocatalytic activity, which demonstrates its high stability. Furthermore, the SEM and TEM images (Fig. S15) demonstrated that the morphology and crystalline phase of the sample after the photocatalytic reaction were not changed, which indicated its high stability.

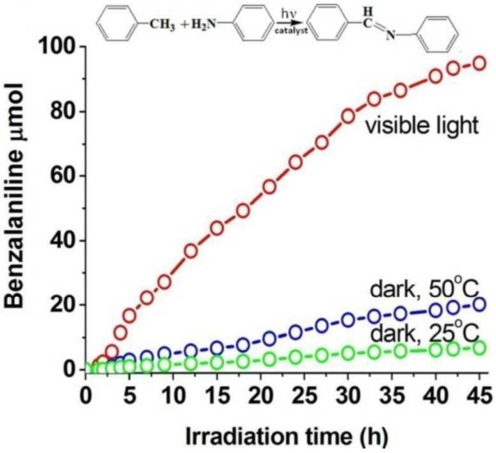

Fig. 5 Time courses of benzalaniline production over the Ag/MoO_3 nanobelts with different reaction conditions.

Table 1: Photocatalytic Coupling of aniline compounds and toluene in the presence of Ag/MoO_3 nanobelts.

Anilines	Main Product	Con (%)	Sel (%)
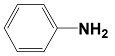	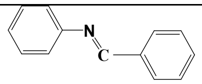	96.8	97.3
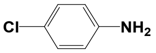	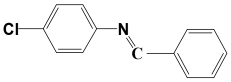	95.6	92.8
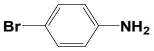	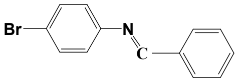	83.2	67.3
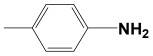	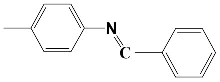	74.5	86.3
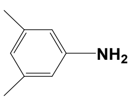	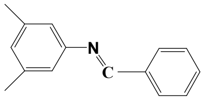	58.6	83.7

Conclusions

In summary, we have developed a facile and general method for direct growth of metal particles on metal oxides. Through an in situ redox reaction between the weakly reductive support and oxidative metal precursors, a series of metal/semiconductor nanocomposites with uniform metal dispersion were obtained. We anticipate that by careful manipulation, this type of room-temperature in-situ growth process can be both a general and highly effective method for improving the surface accessibility of nanoparticles without compromising their deliberately engineered size distribution or morphological characteristics.

Notes and references

[a] Nanomaterials and Nanoproducts Research Center, Chinese Academy of Inspection and Quarantine, No. 11, Ronghua Sough Roude, Beijing, 100176, China.

[b] Department of Chemistry, Capital Normal University, No. 105, North Road, West 3th Ring Road, Beijing, 100048.

† Electronic Supplementary Information (ESI) available: Experimental procedure and supporting figures. See DOI: 10.1039/c000000x/

This work received financial support from the Natural Science Foundation of China (51472226), Dean Fund of CAIQ (2014JK006).

1 M. Turner, V. B. Golovko, O. P. H. Vaughan, P. Abdulkin1, A. Berenguer-Murcia1, M. S. Tikhov, B. F. G. Johnson, R. M. Lambert, *Nature* **2008**, *454*, 981–983.
2 W. L. Yang, Y. Zhang, Y. Hu, J. Zhong, H. B. Wu, X. W. Lou, *Angew. Chem. Int. Ed.* **2012**, *51*, 11501–11504.
3 L. C. He, Y. Liu, J. Z. Liu, Y. S. Xiong, J. Z. Zheng, Y. L. Liu, Z. Y. Tang, *Angew. Chem. Int. Ed*. **2013**, *52*, 3741–3745.
4 M. N. O'Brien, M. R. Jones, K. A. Brown, C. A. Mirkin. *J. Am. Chem. Soc.* **2014**, *136*, 7603–7606.
5 M. Rycenga, C. M. Cobley, J. Zeng, W. Y. Li, C. H. Moran, Q. Zhang, D. Qin, Y. N. Xia, *Chem. Rev.* **2011**, *111*, 3669–3712.
6 C. Wang, Y. Hu, C. M. Lieber, S. H. Sun, *J. Am. Chem. Soc*. **2008**, *130*, 8902–8903.
7 C. M. Cobley, J. Y. Chen, E. C. Cho, L. V. Wanga, Y. N. Xia, *Chem. Soc. Rev*. **2011**, *40*, 44-56.
8 A. A. Herzing, C. J. Kiely, A. F. Carley, P. Landon, G. J. Hutchings, *Science* 2008, **321**, 1331–1335.
9 M. Chen, D. W. Goodman, *Chem. Soc. Rev*. **2008**, *37*, 1860–1870.
10 M. C. Daniel, D. Astruc, *Chem. Rev*. **2004**, *104*, 293–346.
11 F. Porta, L. Prati, *J. Catal*. **2004**, *224*, 397–403.
12 I. Lee, J. B. Joo, Y. D. Yin, F. Zaera, *Angew. Chem. Int. Ed.* **2011**, *50*, 10208-10211.
13 P. Li, Z. Wei, T. Wu, Q. Peng, Y. D. Li, *J. Am. Chem. Soc.* **2011**, *133*, 5660–5663.
14 L. Q. Liu, S. X. Ouyang, J. H. Ye, *Angew. Chem. Int. Ed.* **2013**, *52*, 6689 –6693.
15 Z. W. Seh , S. H. Liu , M. Low , S. Y. Zhang, Z. L. Liu, A. Mlayah, M. Y. Han, *Adv. Mater.* **2012**, *24*, 2310-2314.
16 E. Elmalem, A. E. Saunders, R. Costi, A. Salant,U. Banin, *Adv. Mater*. **2008**, *20*, 4312–4317.
17 R. Abe, H. Takami, N. Murakami, B. Ohtani, *J. Am. Chem. Soc.* **2008**, *130*, 7780–7781.
18 M. Mrowetz, W. Balcerski, A. J. Colussi, M. R. Hoffmann, *J. Phys. Chem. B*. **2004**, *108*, 17269-17273.
19 Z. G. Zhao, M. Miyauchi, *Angew. Chem. Int. Ed.* **2008**, *47*, 7051–7055.

20 X. L. Yan, T. Ohno, K. Nishijima, R. Abe, B. Ohtani, *Chem. Phys. Lett*. **2006**, *429*, 606-610.

21 S. Linic, P. Christopher, D. B. Ingram, *Nat. Mater.* **2011**, *10*, 911–921.

22 E. A. Coronado, E. R. Encina, F. D. Stefani, *Nanoscale* **2011**, *3*, 4042 –4059.

23 L. D. Menard, F. Xu, R. G. Nuzzo, J. C. Yang, *J. Catal.* **2006**, *243*, 64−73.

24 J. A. Lopez-Sanchez1, N. Dimitratos, C. Hammond, G. L. Brett, L. Kesavan, S. White, P. Miedziak, R. Tiruvalam, R. L. Jenkins, A. F. Carley, D. Knight, C. J. Kiely, G. J. Hutchings, *Nat. Chem*. **2011**, *3*, 551-556.

25 W. J. Dong, S. H. Feng, Z. Shi, L. S. Li, Y. H. Xu, *Chem. Mater*. **2003**, *15*, 1941-1943.

26 X. W. Lou, H. C. Zeng, *Chem. Mater*. **2002**, *14*, 4781–4789.

27 X. W. Lou, H. C. Zeng, *J. Am. Chem. Soc*. **2003**, *125*, 2697–2704.

28 Z. Y. Wang, S. Madhavi, X. W. Lou, *J. Phys. Chem. C* **2012**, *116*, 12508–12513.

29 G. C. Xi, S. X. Ouyang, P. Li, J. H. Ye, Q. Ma, N. Su, H. Bai, C. Wang, *Angew. Chem. Int. Ed*. **2012**, *51*, 2395 –2399.

30 T. R. Gordon, M. Cargnello, T. Paik, F. Mangolini, R. T. Weber, P. Fornasiero, C. B. Murray, *J. Am. Chem. Soc*. **2012**, *134*, 6751-6761.

31 Q. Q. Huang, S. Hu, J. Zhuang, X. Wang, *Chem. Eur. J.* **2012**, *18*, 15283-15287.

32 S. E. Skrabalak, J. Chen, L. Au, X. Lu, X. Li and Y. Xia, *Adv. Mater.* **2007**, *19*, 3177-3184.

33 M. Hu, J. Y. Chen, Z. Y. Li, L. Au, G. V. Hartland, X. D. Li, M. Marquez, Y. N. Xia, *Chem. Soc. Rev.* **2006**, *35*, 1084-1094.

34 P. Wang, B. B. Huang,X. Y. Qin, X. Y. Zhang, Y. Dai, J. Y. Wei, M. H. Whangbo, *Angew. Chem. Int. Ed.* **2008**, *47*, 7931 –7933.

35 R. B. Jiang, B. X. Li, C. H. Fang, J. F. Wang, *Adv. Mater.* **2014**, *26*, 5274–5309.

36 M. D. Xiao, R. B. Jiang, F. Wang, C. H. Fang, J. F. Wang J. C. Yu, *J. Mater. Chem. A* **2013**, *1*, 5790-5805.

37 C. L. Wang, D. Astruc, *Chem. Soc. Rev.* **2014**, *43*, 7188-7216.

38 F. Wang, C. H. Li, H. J. Chen, R. B. Jiang, L. D. Sun, Q. Li, J. F. Wang, J. C. Yu, C. H. Yan, *J. Am. Chem. Soc*. **2013**, *135*, 5588–5601.

39 S. T. Kochuveedu, Y. H. Jang, D. H. Kim, *Chem. Soc. Rev*. **2013**, *42* 8467 - 8493

40 Y. J. Lin, S. Zhou, X. H. Liu, S. Sheehan, D. W. Wang, *J. Am. Chem. Soc*. **2009**, *131*, 2772–2773.

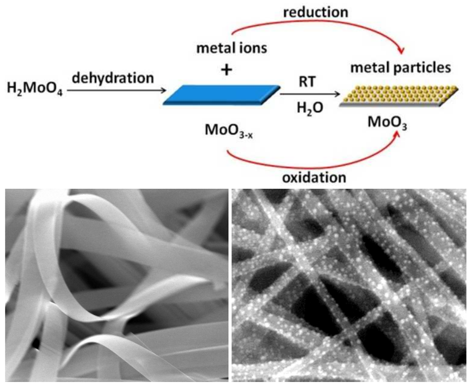

We report a facile method for direct growth of noble-metal nanoparticles on semiconductor nanostructures through an in-situ redox reaction.